Multi-Objective Optimization of an Intelligent Soil-Moisture-Monitoring Satellite Constellation

Ben Gorr[*]
Texas A&M University, College Station, Texas 77843
Vinay Ravindra[†]
NASA Ames Research Center, Moffett Field, California 94035
Amer Melebari[‡]
University of Southern California, Los Angeles, California 90089
Alan Aguilar Jaramillo[§]
Texas A&M University, College Station, Texas 77843
Sreeja Nag[¶]
NASA Ames Research Center, Moffett Field, California 94035
Mahta Moghaddam[**]
University of Southern California, Los Angeles, California 90089
and
Daniel Selva[††]
Texas A&M University, College Station, Texas 77843

https://doi.org/10.2514/1.A35558

In early satellite mission design, requirements are not yet fixed, cost is sometimes negotiable, and designs are relatively unconstrained. During this period of design freedom, multi-objective optimization can provide a useful lens into the design space by showing theoretical performance limits and illuminating design tradeoffs. This work optimizes a radar constellation for a potential soil moisture mission. Several different optimization cases with different variables are considered and contrasted. The optimization of the instrument and constellation parameters is considered jointly and separately to better understand the effect of coupling on the optimization performance. A science-driven optimization based on soil moisture retrieval error is compared with a performance-metric-driven optimization. Pareto analysis and association rule mining are performed on the generated designs to provide insight into driving features. Design recommendations are made for several cost caps. Results show that optimization that considers the instrument and constellation design together find superior revisit metrics than treating instrument and constellation separately. The use of the science value metric as an optimization objective shows that while cost may always be increased to improve instrument and constellation performance, the difference in science value may be negligible. These findings can inform tradespace exploration studies for similar problems.

Nomenclature

A	=	all architectures, tradespace
B_T	=	chirp bandwidth
b	=	bits per pixel
c	=	speed of light
D	=	antenna diameter
d	=	dimension
F	=	feature
F_N	=	receiver noise figure
f	=	focal length
f_P	=	pulse repetition frequency
G_A	=	antenna gain
h	=	orbit height
i	=	inclination
k	=	Boltzmann's constant
L	=	losses
l	=	length
m	=	mass
N	=	number of looks per measurement
n_p	=	number of planes
n_s	=	number of satellites per plane
P	=	power
PF	=	Pareto front
R	=	radar range
r	=	data rate
s	=	swath
sr	=	speckle noise reduction
T	=	target physical temperature
V	=	volume
v	=	velocity
x	=	spatial resolution
Δt_p	=	pulse width
δ	=	antenna depth
ρ	=	density
ψ_g	=	grazing angle

Subscripts

at	=	along-track
atmos	=	atmospheric
avg	=	average
az	=	azimuth
ct	=	cross-track
el	=	elevation
g	=	ground
peak	=	peak
radar	=	radar
s	=	orbital

I. Introduction

IN THE beginning stages of mission design, or Pre-Phase A in NASA terminology [1], the focus of engineers is on exploration of the tradespace. At this point, high-level requirements are still being refined and the precise architecture is yet to be defined. If computational models of the mission's figures of merit (e.g., performance, cost) are available, they can be used in combination with search/optimization and visual/data analytics tools to explore the design space in a rigorous and systematic way. This process is often called tradespace exploration [2]. When design options are discrete and few in number, such as choosing among a small set of predefined instruments (e.g., passive-optical, synthetic aperture radar (SAR), reflectometer) and orbits (e.g., low Earth orbit [LEO], sun-synchronous orbit [SSO], geostationary orbit [GEO]), the full tradespace can be explored via full-factorial enumeration. In continuous spaces, or in discrete spaces with many options, or when the performance models are very computationally expensive, full-factorial enumeration is not feasible, so multi-objective optimization allows engineers to find good designs for a given set of design options. Here we examine evolutionary algorithms as a method of solving the multi-objective optimization problem. While most evolutionary algorithms offer no useful guarantees of optimality, their simplicity and ability to handle arbitrary black-box objective functions and output good solutions at any point during the search has led them to be popular among systems engineers.

Multi-objective optimization has previously been applied to constellation design. Ferringer et al. [3], Hu et al. [4], Xu et al. [5], and Dai et al. [6] all used coverage metrics such as maximum response time and percent coverage to optimize constellation designs for Earth observation. Others have included payload design in the optimization as well [7–11], while others have optimized directly on constellation variables such as repeat cycle and altitude [12]. Saboori et al. [13] considered four different optimization objectives for repeat SSO remote-sensing missions, but only considered two objectives at a time. Pu et al. [14] split a single objective—reward for observing ground points—into two objectives, mean and sum of reward, to conduct a multi-objective optimization for orbit design. Some have included cost modeling in their optimizations [5,7,9], but most ignore cost. This work is unique in including cost, coverage, and instrument metrics (e.g., radar noise equivalent sigma zero) in a single optimization, while previous works consider only one or two of these areas. Additionally, this work is unique in extending the optimization to the actual measurement variable in question, in this case soil moisture retrieval error. While payload performance has been included in previous work, it is either restricted to communication payloads [8,10], the number of images collected [9], or only included as a constraint [7]. This work also shows the difference in optimization solutions between science-driven and instrument performance parameter-driven optimizations. Some work has been done on science-driven tradespace exploration for space mission design [15,16], but this work directly connects the instrument observation metrics with a measurement retrieval model. Because the science-driven optimization is closer to evaluating the true objective of the mission, the difference between these two optimizations may reveal weaknesses in the proxy metrics used in instrument performance parameter optimization.

Here we examine the application of multi-objective optimization to a soil-moisture-monitoring constellation. This soil moisture constellation is based on the work of the D-SHIELD project [17–19], which aims to develop software modules that aid in heterogeneous mission analysis and design. The D-SHIELD project studies the intelligent tasking of instruments, and the motivation for this study was to identify a promising constellation design to study in detail. Soil moisture was chosen as an observable due to its spatiotemporal variability and importance in many geophysical applications. It was envisioned that the soil moisture constellation would be composed of large radars for high accuracy and excellent spatial resolution measurements. Although its design is not considered in this work, a supplementary constellation of radiometers and reflectometers would exist to provide soil moisture information with better temporal resolution than the primary radar constellation.

The multi-objective optimization conducted here proceeds from the most constrained case of a fixed-instrument, fixed-altitude constellation to an unconstrained case of variable instrument parameters and variable altitude. Although the constraints may seem artificial and unrealistic, they are reflective of constraints in engineering practice.

We also examine the structure of the optimization in this work. Motivated by practical interfaces between instrument design and constellation design, we examine the difference between joint optimization including both constellation and instrument design parameters and a separate optimization that considers instrument design followed by constellation design. The utility of this examination is most evident in the effect of altitude on both instrument and constellation design. If the altitude is designed for during the instrument optimization, then the constellation optimization is severely constrained by the predefined altitude.

Soil moisture can be predicted globally, and as a result of missions like Soil Moisture and Ocean Salinity (SMOS) and Soil Moisture Active Passive (SMAP), soil moisture prediction models have only improved. However, there will always be some uncertainty present in the prediction. Quantifying this uncertainty and using it to plan satellite actions to minimize global uncertainty is one of the key focuses of the aforementioned D-SHIELD project. Therefore we seek to design a satellite constellation that gives the *ability* to target areas with the most uncertainty. This objective needs to be balanced with minimizing the retrieval error, which depends on the instrument and operational parameters of the observation, such as look angle.

II. Methods

A. Evaluation

This work considers a satellite constellation composed of large radar satellites, intended for high resolution measurements of soil moisture.

The following subsections describe how the constellation is evaluated. The design variables and design objectives for the optimization are listed in Table 1. A diagram showing the different modules of the evaluation and the major data flows between them is provided in Fig. 1.

Table 1   Radar design variables and objectives

Design variable	Acceptable range
Azimuth dimension (d_{az})	0.1–15 m
Elevation dimension (d_{el})	0.1–15 m
Chirp bandwidth (B_T)	1–80 MHz
Pulse width (Δt_p)	1–1000 μs
Orbit height (h)	300–1000 km
Inclination (i)	45–90 deg
Number of satellites per plane (n_s)	1–5
Number of planes (n_p)	1–4

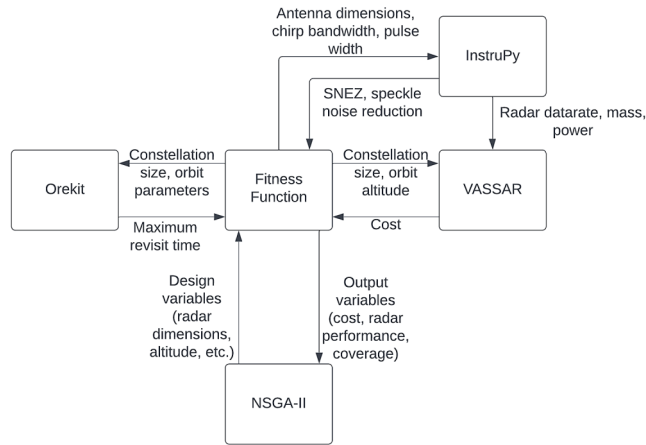| Objective, unit	Min/Max
NESZ, dB	Min
Speckle noise reduction for 1 sq. km. pixel, dB	Max
Cost, FY22\$M	Min
Max. revisit time, h	Min

Fig. 1 Interconnections between evaluation modules.

The antenna dimension limits are artificially low to bias the optimization away from extremely heavy and expensive designs. The chirp bandwidth and pulse width ranges are loosely based on the chirp bandwidth and pulse width of existing SAR systems. The orbit height is limited on the low end by drag considerations and on the high end by degraded SAR performance at higher altitudes. The inclination is limited on the low end by the requirement of viewing the northernmost points of the Earth's landmass. The number of satellites and number of planes are limited to prevent extremely expensive constellations.

This work focuses on the field of regard (FOR) of the observing system, rather than the field of view (FOV) of the instrument. This is due to the D-SHIELD project's focus on intelligent tasking for maneuverable satellites.

Because FOR was considered rather than the FOV of the constellation, maximum revisit time was considered to be more relevant than average revisit time as a design objective, as it is reflective of the capability limit of the system rather than an intermediate value that would not apply to the FOV case.

For the radars, noise equivalent sigma zero (NESZ) is a measure of the sensitivity of the radar and is heavily influenced by both antenna dimensions (azimuth dimension d_{az}, elevation dimension d_{el}), the orbit height, the chirp bandwidth, and the pulse width. Speckle noise in radars is due to interference of multiple wavefronts, and is a significant source of noise in radar observation. It can be reduced by taking multiple observations to average out the noise, i.e., spatial averaging. Therefore speckle noise reduction is a function of the number of looks, which is dependent on the "raw" or native spatial resolution of the observation as well as the choice of the processed pixel size. The smaller the native pixel, the greater the speckle noise reduction. Out of the considered design variables, speckle noise reduction is primarily driven by the antenna azimuth dimension, the chirp bandwidth, and the orbit height. Also considered as variables were the lifecycle cost and the maximum revisit time of the constellation. Lifecycle cost and the radar performance parameters are conflicting objectives, as high performance requires large antennas, which in turn require heavy, expensive satellites. Orbit height greatly affects both radar performance and maximum revisit time, as a high orbit is better for revisit but worse for radar performance.

Also relevant to the radar performance is the look angle. For evaluating the radar performance, we consider a fixed look angle of 45 deg, although the satellite can observe anywhere from 30 to 60 deg. An intelligent scheduler is expected to provide optimal commands; thus the platform needs to be designed for all cases. At 30 deg the NESZ will be best, and at 60 deg the NESZ will be worst. Therefore 45 deg was selected as an average value for the range of look angles.

Orbits with inclinations above 90 deg (i.e., SSO orbits) were excluded due to the one-day timespan of the simulation period. The short simulation time period means that the difference in orbital perturbations experienced by the satellite will be relatively small, so

the coverage results for an inclination of 85 deg should be similar to those with an inclination of 95 deg.

1. Instrument Evaluation

The selected payload is assumed to be an L-band and P-band radar. The L-band radar design can be generalized to a P-band radar, which has been found to be very effective for soil moisture retrieval [20] but has not yet been flown in space. Therefore we design for the L-band case, and assume that the antenna can be shared between the electronics for the P-band and L-band. We assume a mesh reflector antenna inspired by the Microwave Observatory of Subcanopy and Subsurface (MOSS) mission concept [21]. Table 2 shows properties of the radar that are held constant. The maximum of d_{az} and d_{el} is taken to be the diameter of the physical antenna. A rectangular aperture of dimensions d_{az} and d_{el} is illuminated on the surface of the circular mesh. The chirp bandwidth, pulse width, and pulse repetition frequency (PRF) must be carefully selected to avoid overlap of successive radar pulses. The complexity of the relationship between these variables is more fully explored in [22].

The radar performance parameters considered are NESZ and speckle noise reduction, both measured in decibels.

To compute NESZ, the equation from [22] is given below, where k is Boltzmann's constant, T is the target's physical temperature, c is the speed of light, R is the distance from the radar to the target, v_s is the satellite orbital velocity, ψ_g is the grazing angle, B_T is the chirp bandwidth, F_N is the receiver noise figure, L_{radar} is the radar system losses, L_{atmos} is the atmospheric loss, P_{avg} is the average power, G_A is the antenna gain, λ is the operating wavelength, and L_r, L_a, a_{wr}, and a_{wa} are all signal processing losses.

$$\text{NESZ} = \frac{256\pi^3 kT}{c}\left(R^3 v_s \cos\psi_g\right)\left(\frac{B_T F_N L_{\text{radar}} L_{\text{atmos}}}{P_{\text{avg}} G_A^2 \lambda^3}\right)\left(\frac{L_r L_a}{a_{wr} a_{wa}}\right) \tag{1}$$

All parameters in the above equation that relate to the front-end electronics are kept the same for all radar designs. Pulse-width, PRF, and peak power are not explicitly represented in the above equation, but are implicitly represented by P_{avg}.

Therefore the parameters that change with our design variables are captured in the expression below:

$$\text{NESZ} \propto R^3 v_s \cos\psi_g \frac{B_T}{P_{\text{avg}} G_A^2} \tag{2}$$

Note that ψ_g is a function of the altitude and look angle. The altitude may vary but the look angle is assumed to be 45 deg.

To compute speckle noise reduction is much simpler. Computation of the speckle noise reduction for a 1 sq. km. pixel relies on the pixel size of the radar observation. The cross-track spatial resolution in meters is given by the following equation:

$$x_{\text{ct}} = \frac{a_{wr} c}{2 B_T \cos\psi_g} \tag{3}$$

The along-track spatial resolution x_{at} in meters is given by the following equation, where v_g is the satellite ground speed in meters per second:

Table 2 Radar design constants

Parameter	Value
Center frequency	1.2757 GHz
Minimum PRF	1 Hz
Maximum PRF	20,000 Hz
Peak transmit power	1000 W
Swath (fixed)	25 km

$$x_{\text{at}} = \frac{d_{\text{az}}}{2}\frac{v_g}{v_s} \tag{4}$$

From these two values, we arrive at an equation for the speckle noise reduction sr, in decibels:

$$sr = 10\log\sqrt{\frac{x_{\text{at}}x_{\text{ct}}}{10^6}} \tag{5}$$

This speckle noise reduction corresponds to a 1 km^2 processed pixel size, hence the 10^6 in the equation.

2. Coverage Evaluation

To evaluate the coverage of the constellation, the Orekit flight dynamics library [23] was used. A one-day simulation time was used. The grid used for coverage calculations was of 5 deg granularity (selected based on Fig. A1 in the Appendix) over the Earth's land-masses, because soil moisture is only relevant on land. The short simulation duration and coarse grid granularity were practical limitations on the evaluation runtime; however, a brief convergence analysis showed that results did not differ significantly from finer grids and longer runtimes. The propagator used was a two-body Keplerian propagator. A two-body or Keplerian propagator is much faster than more complex propagators including perturbations, but is less accurate for longer simulation durations and will not accurately capture repeat ground track orbits. Figure A2 in the Appendix shows the sensitivity of the maximum revisit time metric to simulation duration and propagator type for several example orbits. As can be seen, the results from the one-day Keplerian propagation differs from the more accurate J2 propagation, with a mean error of 4.9% (error ranges between 0.8 and 27.7%). The highest error is observed for a constellation of 4 satellites in 4 planes ("4/1 500 km 75 deg"), propagated for 10 days. Future work should use higher-fidelity propagators and longer simulation times if computation time permits.

The percent coverage and maximum revisit time were computed over a one-day simulation time. The reported maximum revisit time is the highest maximum revisit time for all points considered. It should be noted that this maximum revisit time is not the "true" maximum revisit time but is rather the maximum revisit time for points seen at least twice within a 24 h time period. These results can be very different from the true maximum revisit time, because there is an iso-cost tradeoff between coverage and revisit. Only architectures with 100% coverage are included in the output, so there are no unobserved points. This 100% coverage is driven by a mission-level requirement for being capable of observing any point on Earth within a day.

A Walker Delta constellation design [24] was used to establish the satellite constellation. The phasing parameter was set to 1, and only circular orbits were considered. The phasing parameter and eccentricity were considered to be of negligible importance to the trades-pace. The exclusion of elliptical orbits from the design space is motivated by the fact that radar returns are heavily dependent on orbit altitude, and so a varying orbit altitude would be very challenging from an instrument perspective.

Because the radar satellite is assumed to be agile, the FOR was used to compute the coverage metrics. In this case, the FOR was the set of angles $[-60, -30] \cup [30, 60]$ deg from nadir. This FOR represents scanning in the cross-track direction.

3. Cost Evaluation

Because the cost of the constellation is a function of not only the satellite cost but also launch, operations, integration, assembly, and test (IA&T) and programmatic costs, we must have some method of evaluating these costs.

Here we turn to the Value Assessment of System Architectures Using Rules (VASSAR) rule-based architecture evaluation tool [25]. VASSAR takes a set of instruments and the orbit they are assigned to as an input, sizes a satellite bus to meet the requirements of the payload in that orbit (i.e., mass, power, data rate, physical dimensions), and then selects a launch vehicle capable of transporting the

resulting set of spacecraft to the specified orbit. It also estimates development, operational, and programmatic costs to produce a life-cycle cost for the entire mission using Cost Estimation Relationships from the Unmanned Spacecraft Cost Model 8 (USCM8) [26]. This mission lifecycle cost is the "cost" mentioned from here onward.

For VASSAR to be able to evaluate an architecture, the mass, power, and data rate of the payload must be specified. By payload we mean a collection of instruments, in this case the L- and P-band radars.

4. Radar Design

To determine the mass of the radar instrument, we partially relied on the MOSS radar design in [27].

We assume that the feed length is approximately proportional to the antenna length. Using the MOSS radar feed length of 3.3 m for an antenna length of 30 m, the feed length for a radar is given in Eq. (6).

$$l_{\text{feed}} = \frac{3.3}{30}l_{\text{antenna}} \tag{6}$$

Assuming that the feed width is one-third of the feed length, and that the feed height is 0.05 m, we arrive at Eq. (7) for the mass of the feed. We assume that the feed bulk density is $\rho_{\text{feed}} = 590$ kg/m^3, based on MOSS [27].

$$m_{\text{feed}} = \rho_{\text{feed}}V_{\text{feed}}\max(d_{\text{az}}, d_{\text{el}}) \tag{7}$$

For the reflector design, we assume an f/D (ratio of focal length to diameter) of 0.45. Equation (8) is the focal length equation for prime focus antennas.

$$f = \frac{D^2}{16\delta} \tag{8}$$

Using the above equation and assuming that $\rho_{\text{refl}} = 0.151$ kg/m^3, based on MOSS [27], we arrive at Eq. (9) for the reflector (mesh +antenna) mass.

$$m_{\text{refl}} = \rho dr^2 = d\rho_{\text{refl}}\pi\left(\frac{\max(d_{\text{az}}, d_{\text{el}})}{2}\right)^2 = \rho_{\text{refl}}\pi\frac{\max(d_{\text{az}}, d_{\text{el}})^3}{28.8} \tag{9}$$

To establish a relationship for the mass of the radar electronics, regression was performed on the radars in Table 3.

The following equation was produced, with an R^2 value of 0.568. A lower bound constraint was introduced to ensure that negative masses could not be generated for peak powers below 10.56 W.

$$m_{\text{elec}} = 21.253\ln(P_{\text{peak}}) - 50.093 \tag{10}$$

We can now combine Eqs. (7), (9), and (10) to obtain the total mass of the radar instrument.

$$m_{\text{radar}} = m_{\text{feed}} + m_{\text{refl}} + m_{\text{elec}} \tag{11}$$

Finally, to determine the data rate r of the instrument, we use Eq. (12), where b is the number of bits per pixel, s is the swath size, x_{ct}

Table 3   SARs used for regression

Radar	Electronics mass, kg	Peak power, W
SMAP	56	500
ALOS-2	109.1	3300
MAPSAR	193.6	1000
PALSAR	100	2000
SAOCOM-SAR	100	3100
MicroSAR	2.5	35
UAVSAR	100	2000
GAMMASAR	7.56	10

is the pixel size in the cross-track direction, N is the number of looks per measurement, v_g is the ground speed of the satellite, and x_{at} is the pixel size in the along-track direction.

$$r = b \frac{s}{x_{ct}\sqrt{N}} \frac{v_g}{x_{at}} \quad (12)$$

For this work, the peak power of the radar is assumed to be 1000 W, and the average power consumption P_{avg} is based on the PRF f_P and pulse width Δt_p, as shown in Eq. (13).

$$P_{avg} = P_{peak} f_P \Delta t_p \quad (13)$$

To allow for improved retrieval of soil moisture, a P-band radar was included on every satellite with an L-band radar. This P-band radar used the same antenna system, so the only change was an additional electronics mass of 96.71 kg to support P-band measurements. The 96.71 kg mass is based on Eq. (10) with a peak power of 1000 W.

5. Instrument Cost Estimation

Having obtained the instrument characteristics, we now turn to the NASA Instrument Cost Model (NICM) [28] to obtain the cost of the payload in FY04$M.

$$\text{cost}_{ins} = 25600 \left(\frac{p}{61.5}\right)^{0.32} \left(\frac{m_{radar}}{53.8}\right)^{0.26} \left(\frac{r}{40.4}\right)^{0.11} \quad (14)$$

For an example radar with a mass of 170.55 kg, an average power of 100 W, and a data rate of 827.7 kbps, this formula yields a cost of 50.1 FY04$M, or 77.5 FY22$M accounting for inflation.

6. Mission Cost Estimation

The mission lifecycle cost was computed for a 5-year mission, and includes all aspects of cost, including spacecraft cost, integration, assembly and testing (IA&T), operations, launch, and program overhead.

The program, IA&T, and operations cost are all proportional to the mass of the spacecraft. The automated scheduling produced by the D-SHIELD project does not add extra cost to the mission. The launch cost is determined by more complex rules that determine the cheapest launch manifest by slotting satellites into the launch vehicles given in Table 4.

A mass budget and cost breakdown, both obtained from VASSAR, for a satellite with the above example radar are shown in Tables 5 and 6.

7. Science Value

The NESZ and number of looks for the radar were determined and input to a soil moisture retrieval model, which returned the retrieval error, specifically the root-mean-squared error (RMSE), for various biomes as a function of observation geometry. The soil moisture retrieval model is detailed in [18]. It considers the normalized radar cross section (NRCS) of the instrument and uses an optimizer and forward model to complete the retrieval. A random sampling of International Geosphere-Biosphere Programme (IGBP) grid points

Table 4   Launch vehicles considered

Launch vehicle	Cost, FY00$M
Ariane 5 ESCA	100
Soyuz	45
Vega	20
SLS	500
Delta-7320	45
Delta-7420	55
Delta-7920	65
Taurus-XL	30
Minotaur-IV	35

Table 5   Satellite mass budget

Subsystem	Mass, kg
ADCS	57.7
Avionics	52.5
Comms	9.5
EPS	110.7
Payload	170.6
Structure	148.5
Propulsion	8.6
Other	7.0
Total dry mass	**562.9**

Table 6   Mission cost

Cost contributor	Amount, FY22$M
Payload cost	54.9
Satellite bus cost	109.1
Program cost	62.6
IAT cost	28.0
Operations cost	30.5
Launch cost	37.7
Lifecycle cost	**322.8**

was used as the set of coverage points. These IGBP grid points all have an associated biome, such as savanna or mixed forest. It was assumed that soil moisture retrieval error will be similar within biomes, but not across biomes. The error for each grid point was set to the retrieval error for the biome corresponding to that specific point. Because the percent coverage in one day was constrained to 100, the soil moisture error was simply the sum of the retrieval errors over all of the grid points.

B. Optimization

To perform this optimization, a genetic algorithm was used because it is a popular tool thanks to the flexibility and performance of the algorithm in practice.

1. Genetic Algorithm

The NSGA-II algorithm [29] was used for multi-objective optimization. While NSGA-II is an older algorithm, it is widely used in practice (e.g., [3,6,8]). More modern algorithms like NSGA-III focus on improving performance for many objectives (i.e., >4), which is not the case in this work. The algorithm implemented was the default NSGA-II algorithm in the Java MOEA Framework, terminated at 2700 function evaluations, with a population size of 100. This number of function evaluations is relatively low, but results (e.g., Fig. A3 in the Appendix) suggest that it is sufficient for convergence. The settings for the NSGA-II algorithm, taken from the default settings from the aforementioned Java framework, are given in Table 7.

2. Optimization Cases

There were several slices of the tradespace that were relevant to this work. These were treated as separate optimization cases, and are enumerated below. Each of them represents constraints on optimization that may occur in practical mission design. For example, an instrument design or an orbit height may be specified to an engineer before they begin work. While these constraints on design may seem artificial, they occur commonly in practice (e.g., to reuse an instrument

Table 7   NSGA-II settings

Setting	Value
Crossover rate	1.0
Distribution index	15.0
Polynomial mutation rate	0.021
Polynomial mutation distribution index	20.0

or to be part of an existing constellation, respectively). These cases also help focusing the tradespace exploration efforts to smaller, more manageable regions of the tradespace that subject matter experts believe to be more promising.

Case 1 (fixed radar, fixed altitude): The first optimization case was the simplest case—a radar constellation at 500 km altitude with a single instrument design. The 500 km altitude was seen as a compromise between radar power, coverage, and drag. This provided a useful baseline from which to expand our search space. This case used a radar design from a previous optimization study.

Case 2 (variable radar, fixed altitude): The second optimization case allowed the radar instrument design to be varied, but not the altitude. This allowed for cost to be traded for improved radar performance.

Case 3 (variable radar, variable altitude): The third optimization case allowed for the radar instrument design and altitude to be varied. This greatly opened up the possible performance of the constellation, as an instrument designed for an orbit height of 300 km would be much different from one designed for 1000 km.

Case 4 (variable radar, variable altitude, science value): The fourth and final optimization case used a science value metric described above, which helps to connect the radar constellation with the desired observable for the mission, rather than using proxies such as coverage and instrument performance.

Table 8 shows the design variables for the optimization cases.

3. Separate Versus Combined Optimization

One area of interest for this work was the value of jointly optimizing the instrument and orbit designs as opposed to conducting separate optimizations. Because high-fidelity instrument design and orbit design can be very computationally expensive, minimizing the number of function evaluations needed to find good designs is a highly relevant topic to many engineers, and decomposition is a typical heuristic strategy to accelerate convergence [30]. However, the quality of this heuristic depends on the extent to which the two problems are coupled.

For cases 2 and 3 mentioned above, we ran the NSGA-II genetic algorithm to design the instruments first, and then fed the final population into a separate genetic algorithm for the orbit design. These two cases were selected as they varied the instrument parameters and had the instrument performance as objectives. The results of this two-step optimization were compared to an optimization over the entire (instrument+orbit) design space. Cases 2 and 3 were selected as examples, although the method could be applied to case 4 as well.

C. Analysis

Because drawing conclusions from visualizing tradespace plots can be time-consuming and fraught with bias, data mining techniques such as association rule mining are often used [31] to determine more consistently the features that drive the tradespace. Association rule mining seeks to identify design feature (i.e., values of one or more design variables) that are statistically associated with regions of interest in the tradespace A, typically the Pareto front PF. The term "Pareto front" in this work is taken to be the set of nondominated solutions and

Table 8   Comparison of the optimization runs

Case	Design variables	Design objectives
1	n_s, n_p, i	Cost, max revisit
2 (joint)	$d_{az}, d_{el}, B_T, \Delta t_p, n_s, n_p, i$	Cost, max revisit, NESZ, speckle noise reduction
2 (separate)	$(d_{az}, d_{el}, B_T, \Delta t_p)$, (n_s, n_p, i)	Cost, max revisit, NESZ, speckle noise reduction
3 (joint)	$d_{az}, d_{el}, B_T, \Delta t_p, n_s, n_p, i, h$	Cost, max revisit, NESZ, speckle noise reduction
3 (separate)	$(d_{az}, d_{el}, B_T, \Delta t_p, h)$, (n_s, n_p, i)	Cost, max revisit, NESZ, speckle noise reduction
4	$d_{az}, d_{el}, B_T, \Delta t_p, h, n_s, n_p, i$	Cost, soil moisture retrieval error

Table 9   Features used for the "apriori" algorithm

Variable	Comparator	Values/thresholds
n_s	=	1,2,3,4,5
n_p	=	1,2,3,4
i	>	40,50,60,70,80
B_T	>	50,60,70
Δt_p	>	10,20,30,40,50,60,70,80,90
d_{az}	>	14
d_{el}	>	14

should not be considered the "true" Pareto front. These associations are often expressed in the form of rules, e.g., Paretofront $\rightarrow n_s = 4$.

The "apriori" algorithm iteratively constructs candidate features as conjunctions of one or more base features defined in Table 9 and evaluates them based on a number of so-called importance measures. The features in Table 9 were based on subject matter expertise. Support for a given feature F is defined in Eq. (15).

$$\text{support} = \frac{\text{cardinality}(F \cap PF)}{\text{cardinality}(A)} \quad (15)$$

Confidence($F \rightarrow PF$) (also known as specificity), confidence($PF \rightarrow F$) (also known as coverage in the literature), and lift for an association rule are given by Eqs. (16–18).

$$\text{confidence}(F \rightarrow PF) = \frac{\text{supp}(F \cap PF)}{\text{supp}(F)} \quad (16)$$

$$\text{confidence}(PF \rightarrow F) = \frac{\text{supp}(F \cap PF)}{\text{supp}(PF)} \quad (17)$$

$$\text{lift} = \frac{\text{supp}(F \cap PF)}{\text{supp}(PF)\text{supp}(F)} \quad (18)$$

In the context of this study, support essentially indicates the prevalence of the feature within the entire tradespace. Coverage is a measure of the conditional probability that a design on the Pareto front has the feature (i.e., $Pr(F|PF)$). Specificity is a measure of the conditional probability that a design with the feature is on the Pareto front ($Pr(PF|F)$). Lift measures the degree of statistical independence between P and F by calculating the ratio between $Pr(F|PF)$ and $Pr(F)$ or equivalently between $Pr(PF|F)$ and $Pr(PF)$. A lift greater than 1 indicates that a statistical association is likely between PF and F.

The apriori algorithm starts by calculating the importance measures for the base features. Base features that do not meet threshold values for the importance measures are pruned out. With the remaining ones, candidate features of order 2 are created by conjunction of two base features, and evaluated according to the importance measures. More rules are pruned out. The algorithm proceeds iteratively to evaluate features of degree 3 and higher until no more candidate features can be found.

To mine the rules, we used the apriori algorithm [32] using the features given in Table 9. The apriori algorithm was selected over other rule-mining algorithms for its simplicity and ease of use. The threshold for support was 0.05, the threshold for coverage was 0.3, the threshold for lift was 1, and the maximum feature length was 2.

III.   Results

It is the nature of multi-objective optimization to never produce one ideal architecture, but rather to show the limits of performance for a given design space and produce architectures that optimally trade conflicting objectives. The following results show all generations of the optimizations, i.e., the entire evaluated tradespace of 2700 architectures per case, highlighting the Pareto fronts, or nondominated solutions, for the tradespaces considered. A hypervolume analysis is

also conducted on the optimization results. For the purposes of discussion, several architectures on the Pareto front are considered. One obvious way of narrowing down the architectures is to introduce a cost cap. By doing so, we may choose the best architecture that is under the cost cap. This basic heuristic allows us to essentially reduce the number of dimensions in the objective space by 1. We examine the following cost caps: 1.116FY22\$B, from the 915FY15\$M cost of SMAP, and 629.3FY22\$M, from the 469FY09\$M of SMOS. In addition to using these cost caps to select architectures, compromise between the objectives was also considered.

A. Radar Optimization

1. Fixed Instrument, Fixed Altitude

This is the simplest case, only varying constellation topology (n_s, n_p, i). Out of 75 unique architectures, 10 are on the Pareto front. All of these architectures hold the radar instrument performance constant at NESZ of -37.29 dB and a speckle noise reduction of -13.5 dB, because the instrument design is fixed.

Table 10 shows one selected architecture on the Pareto front. This architecture represents a tradeoff between cost and revisit, but as we will see in later sections, is suboptimal. There are no architectures below the cheaper cost cap for this case, due to the improved performance of the baseline instrument over SMOS. As n_s and n_p are increased, maximum revisit time improves at the expense of cost, as shown in Fig. 2a.

Association rule mining for the Pareto front yields the features listed in Table 11. In this and following tables, the top 3 features sorted by lift are shown. The features identified reflect the presence of many four satellite architectures on the Pareto front, and suggest differentiating variables within those architectures.

Figure 3 also suggests that it is expensive to achieve low maximum revisits for this instrument at this altitude, which motivates the expanded searches that follow.

2. Variable Instrument, Fixed Altitude

This case keeps the altitude fixed at 500 km but allows for the instrument design variables to be changed. The instrument objectives are added, for a total of four objectives. Out of 804 unique architectures, 409 of those are on the 4D Pareto front. This is an example of the well-known limited discriminatory power of the Pareto filter for larger numbers of objectives. We therefore look at the 2D Pareto fronts resulting from considering two out of the four objectives. Note that a design that is in any of the 2D Pareto fronts will be in the

Table 10 Selected architectures from the fixed-instrument, fixed-altitude optimization

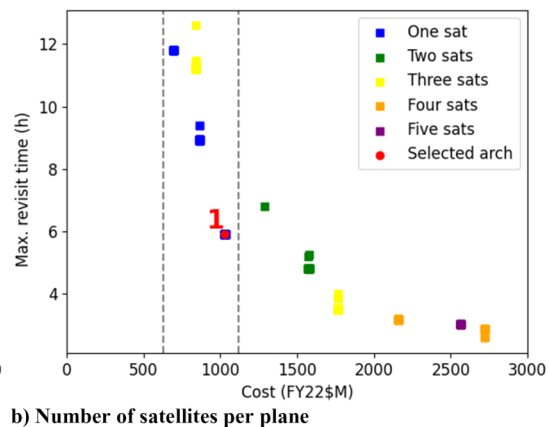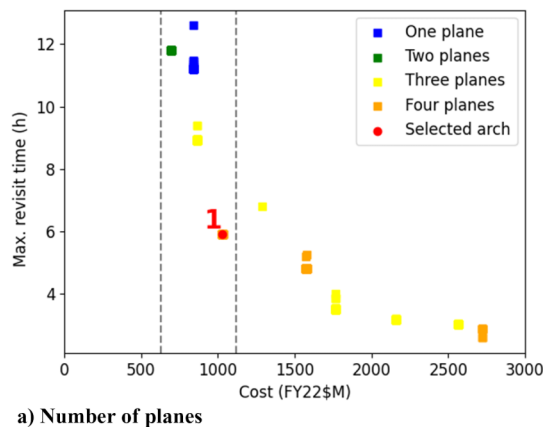| Architecture no.	n_s	n_p	i, deg	Cost, FY22\$M	Max. revisit time, h
1	1	4	80.7	1028.5	5.90

Table 11 Features for the fixed-instrument, fixed-altitude case

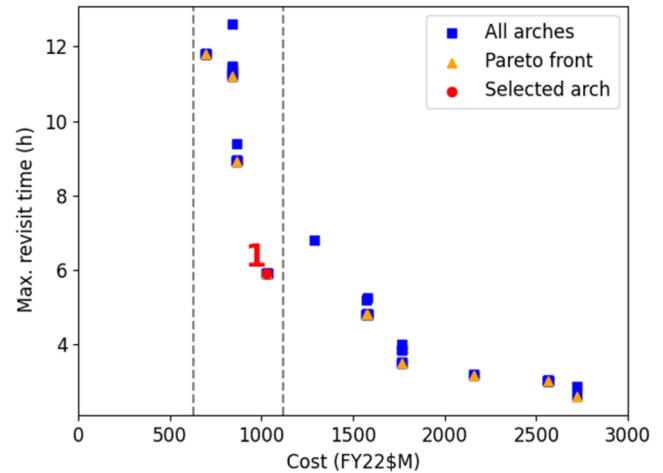| Feature	Support	Lift	Coverage	Specificity
$n_s = 4$ and $n_p = 3$	0.089	1.60	0.889	0.159
$n_s = 4$ and $i > 70$ deg	0.089	1.60	0.889	0.159
$n_s = 4$	0.114	1.46	0.816	0.205

Fig. 3 Architectures for the fixed-instrument, fixed-altitude case, with vertical lines showing SMOS and SMAP cost caps.

original 4D Pareto front, but the opposite is not true, so this is just a subjective decision heuristic to help reduce the space of alternatives, similar to establishing weights between conflicting objectives. While there are six 2D Pareto fronts, in Figs. 4a and 4b, we show only two of the more interesting Pareto fronts for brevity. As an example, there are 86 architectures on the cost-maximum revisit Pareto front.

Because the fixed instrument in case 1 was on the Pareto front of an instrument-only optimization, and here we are freshly optimizing the instrument parameters and thus searching a larger space, the Pareto front for cost and revisit for this case is dominated by the previous case. However, we see from the cost versus NESZ plot that superior radar performance (8 dB improvement) can be obtained at reasonable costs (<\$1B)—see Architectures 2 and 3 in Fig. 4b and Table 12. Architecture 2 offers a slightly improved maximum revisit time for slightly worse NESZ when compared to Architecture 3.

Association rule mining for the 4D Pareto front yields the features shown in Table 13. The selected features show an interesting preference for longer Δt_p and large d_{el}. This preference for larger d_{el} pushes the optimization toward heavier and more costly architectures.

Figure 5 shows the effect of the number of planes and satellites per plane on the tradespace. As can be seen from the difference between
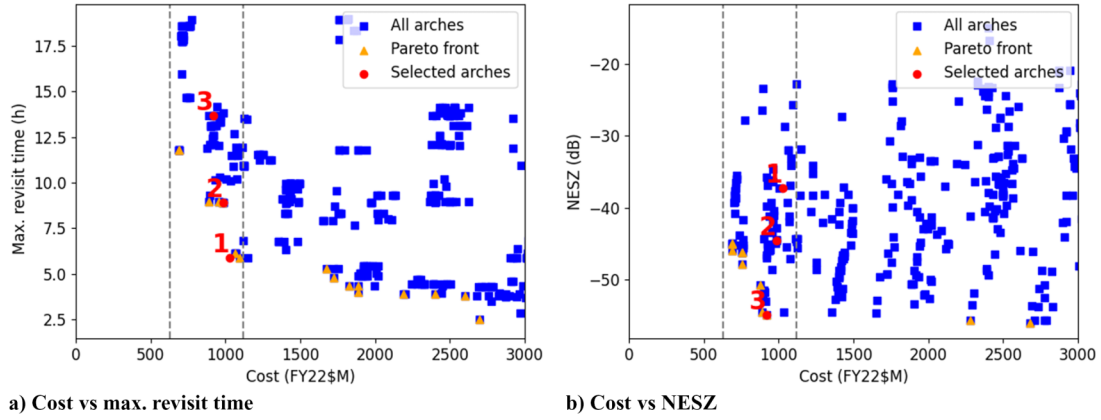

a) Number of planes

b) Number of satellites per plane

Fig. 2 Two specific design variables for case 1, with vertical lines showing SMOS and SMAP cost caps.

a) Cost vs max. revisit time   b) Cost vs NESZ

Fig. 4   Architectures for the variable-instrument, fixed-altitude case, with vertical lines showing SMOS and SMAP cost caps.

Table 12   Selected architectures from the variable-instrument, fixed-altitude optimization

Architecture no.	n_s	n_p	i, deg	d_{az}, m	d_{el}, m	B_T, MHz	Δt_p, μs	Cost, FY22$M	Max revisit time, h	NESZ, dB
2	1	3	75.5	12.7	14.0	21.6	56.2	985.5	8.93	−44.6
3	1	3	70.3	12.8	14.6	1.60	33.5	917.6	13.7	−55.0

Table 13   Selected features for the variable-instrument, fixed-altitude case

Feature	Support	Lift	Coverage	Specificity
$\Delta t_p > 40$ μs and $d_{el} > 14$ m	0.106	1.22	0.867	0.155
$\Delta t_p > 30$ μs and $d_{el} > 14$ m	0.110	1.21	0.865	0.176
$B_T > 50$ MHz and $\Delta t_p > 30$ μs	0.102	1.19	0.852	0.142

the maximum revisit time for architectures with two planes and those with four planes, increasing the number of planes is much more effective than increasing the number of satellites per plane at reducing maximum revisit time.

3. Variable Instrument, Variable Altitude

Here we explore the full design space. Out of 646 unique architectures, 491 are on the 4D Pareto front.

Figure 6 shows the architectures for Case 3, comparing cost against both maximum revisit time and NESZ. Comparing to the previous two cases, we see that a very low maximum revisit time is available at a much lower cost than either of the previous two cases. However, these solutions on the cost/revisit Pareto front have poorer performance than our fixed-instrument design.

Interestingly, we find that the best NESZs found for the variable-altitude case are worse than those of the fixed-altitude case. This is

perhaps because the optimizations were terminated at the same iteration, and the variable-altitude case had a larger search space to explore. This can be seen in Fig. 7, where case 3 continues to improve longer than case 2. An additional possible explanation is the greater coupling between design variables present in the variable-altitude case. Because all of the objectives are greatly affected by the altitude of the constellation, the algorithm is slow to find the designs with the best NESZs.

Table 14 shows selected architectures from this case, selected subjectively to compromise between the four objectives. As can be seen from the previous Pareto fronts, radar performance cannot be greatly improved by increasing cost, as we reach the upper constraints of the design space. What can be achieved with the higher cost cap is a great improvement in maximum revisit time, from 8.50 to 3.65 h. The bulk of this cost increase comes from increasing the number of planes to 2, resulting in a four-satellite constellation.

Association rule mining for the cost/revisit Pareto front yields the following features. Here we see higher lifts than features for the other cases, and lower supports, indicating more narrow features shown in Table 15.

Because we have introduced these three optimization cases for the radar constellation, it seems appropriate to compare the results across the three cases to better understand the effect that the openness of the design space has on the results. This comparison is shown in Fig. 8.

From the cost versus maximum revisit time plot, we see that the third optimization case outperforms the other two strategies. This is
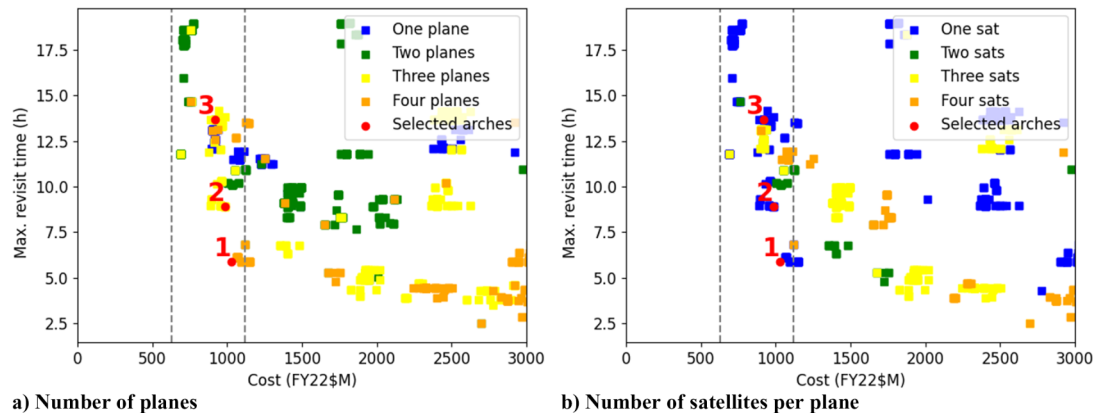

a) Number of planes   b) Number of satellites per plane

Fig. 5   Two specific design variables for case 2, with vertical lines showing SMOS and SMAP cost caps.

a) Cost vs max. revisit time   **b) Cost vs NESZ**
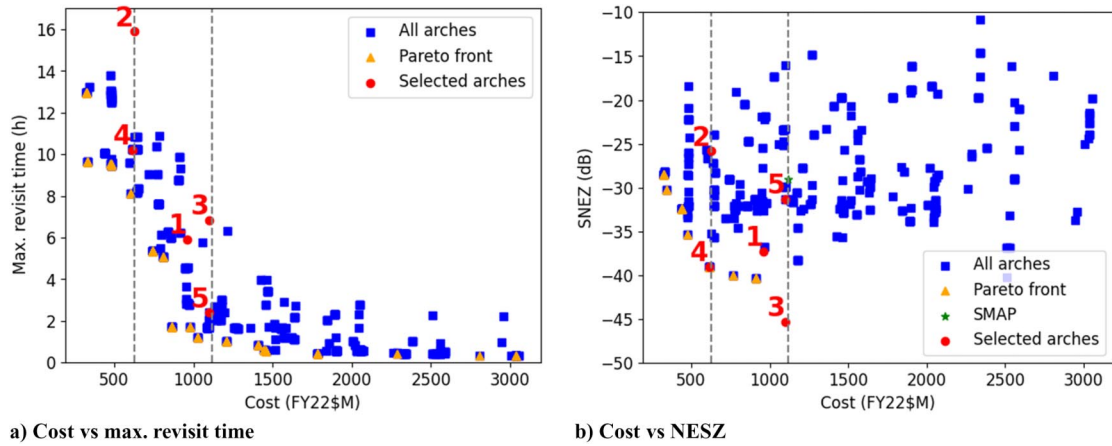
Fig. 6   Architectures for the variable-instrument, variable-altitude case, with vertical lines showing SMOS and SMAP cost caps.
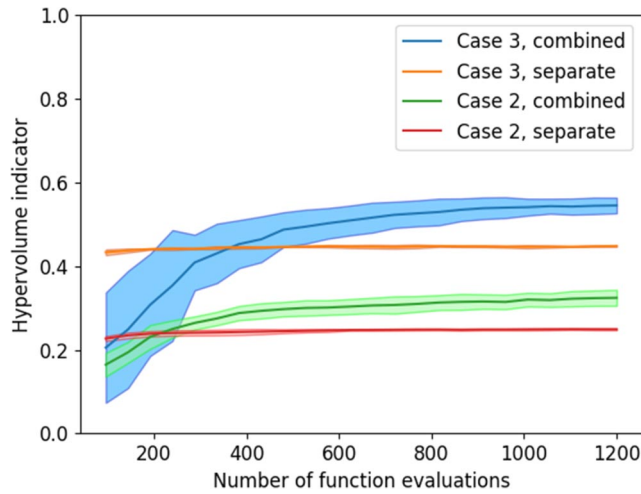

Fig. 7   Hypervolume indicators for the two optimization strategies.

expected because higher altitude orbits allow for greatly improved revisit metrics. The cost versus NESZ plot yields a slightly unexpected result. The combined Pareto front is composed of architectures from both the second and third optimizations. At the cheaper end of the tradespace, varying the altitude allowed for cheaper but still effective constellations. The second optimization case outperforms in a narrow portion of the tradespace. This is possibly due to the genetic algorithm having more function evaluations to explore optimal radar designs without the complicating variable of altitude. Because the second tradespace is a subset of the third tradespace, we know that if the simulation was run for a much longer period of time, eventually the third optimization case would find the same architectures and potentially even better ones, but because the run was truncated at 2700 NFEs, both optimizations have their advantages.

B.   Separate Versus Combined Optimization

1.   Tradespace Analysis

The tradespaces produced by the separate and combined optimization strategies are shown in Fig. 9. These are 2D Pareto fronts based on the last population of the second optimization stage. Figure 9a shows that the combined optimization is able to improve on revisit time, which is to be expected, because the separate optimization does

Table 15   Features for the variable-instrument, variable-altitude case

Feature	Support	Lift	Coverage	Specificity
$n_s = 5$ and $n_p = 4$	0.019	1.629	0.213	0.144
$n_s = 2$ and $n_p = 2$	0.019	1.608	0.210	0.148
$n_s = 2$ and $i > 70$ deg	0.028	1.518	0.199	0.216

not have access to revisit time until the constellation optimization portion. For example, radar design variables cannot be modified to maximize coverage. Figure 9b shows a more mixed result: the separate optimization Pareto front is not completely dominated by the combined optimization. This is perhaps due to the smaller tradespace available to the instrument optimization, which allows it to hone in more quickly on optimal NESZ designs. Table 16 shows two Pareto front architectures. These architectures suggest that the separate optimization did not find large radar designs at low altitudes, potentially because these architectures necessitate more satellites to achieve the 100% coverage requirement.

2.   Hypervolume Computation

While examining the Pareto fronts is a qualitative way of comparing the optimization strategies, a more quantitative measure is the hypervolume indicator [33], which measures both convergence (i.e., quality) and diversity of a set of designs or solutions. To compute the hypervolume indicator, or s-metric, the objectives were normalized using the minimum and maximum objective values for the entire simulation run. To compare across the different optimizations, the objective spaces were combined before the normalization was performed. Because all objectives were normalized, the reference point for the hypervolume indicator calculation was set to [1,1,1,1]. The hypervolume was computed using Eq. (19), where S is the set of points on the Pareto front, r is the reference point, and Λ is the Lebesgue measure, where $[p, r]$ denotes the hypercube delimited by p and r. The reference point is chosen using the anti-utopia point of the 4D objective space. Intuitively, the hypervolume indicator is the volume of the hypercube that is taken up by the 4D Pareto front.

$$H(S) = \Lambda\left(\bigcup_{p \in S}[p, r]\right) \tag{19}$$

Table 14   Selected architectures from the variable-instrument, variable-altitude optimization

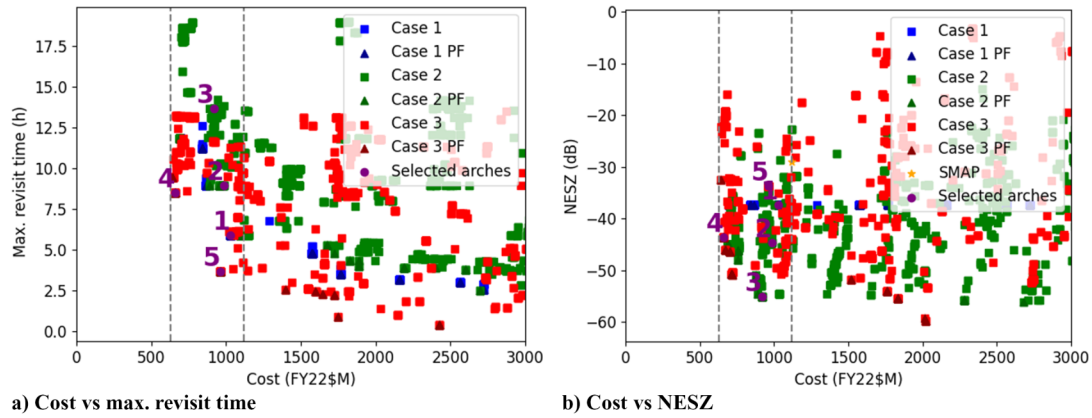| Architecture no.	n_s	n_p	h, km	i, deg	d_{az}, m	d_{el}, m	B_T, MHz	Δt_p, μs	Cost, FY22$M	Max revisit time, h	NESZ, dB	Speckle noise reduction, dB
4	2	1	961.6	45.9	7.79	14.7	1.09	23.5	657.1	8.50	−43.6	−15.8
5	2	2	935.4	76.7	9.66	10.2	12.0	36.5	963.0	3.65	−33.8	−20.6

a) Cost vs max. revisit time   b) Cost vs NESZ

Fig. 8 Comparison of the architectures produced by three optimization cases, with vertical lines showing SMOS and SMAP cost caps.

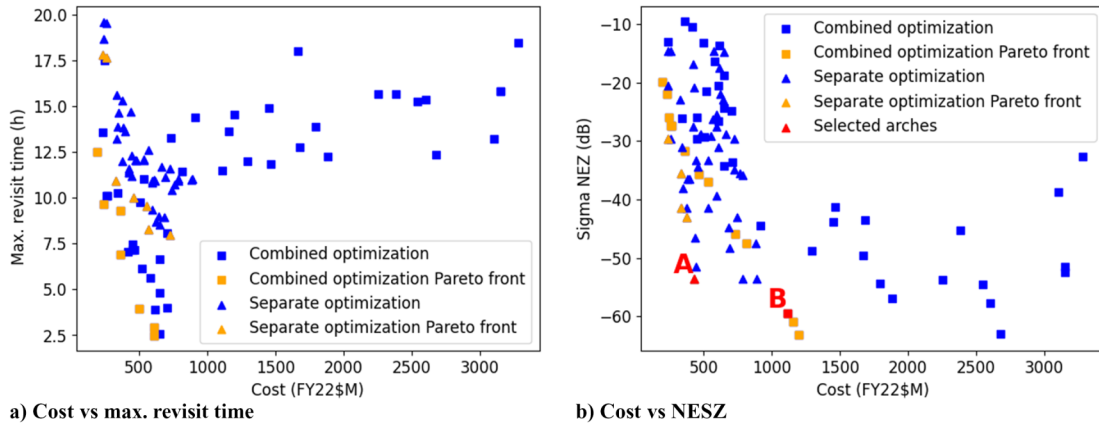a) Cost vs max. revisit time   b) Cost vs NESZ

Fig. 9 Comparison of the combined and separate optimizations for varying altitude radar constellations (case 3).

Table 16   Selected architectures from the separate and combined optimizations

Architecture no.	n_s	h, km	i, deg	d_{az}, m	d_{el}, m	B_T, MHz	Δt_p, µs	Cost, FY22$M	Max revisit time, h	NESZ, dB	Speckle noise reduction, dB
A	3	460	83.6	14.9	6.22	1.01	56.6	428.1	11.6	−53.6	−14.1
B	5	368	89.7	14.9	13.5	2.12	55.2	1113.0	11.5	−59.4	−15.7

Figure 7 shows that the combined optimization is able to more quickly explore and exploit the tradespace than the separate optimization, and continues to improve results over time, while the separate optimization converges to a suboptimal solution. The shading in the figure shows one standard deviation for 10 runs of each case. It is also clear from the figure that the separate optimization converges faster. This is expected as the separate optimization uses decomposition and thus ignores couplings between instrument variables and orbit variables.

Part of the reason for this performance gap is that the choice of altitude is critical to the design of the radar and the design of the constellation, as it heavily affects all objectives. When we fix the altitude, the advantage of the combined optimization is reduced, by approximately 0.05 when we examine the difference in the final hypervolume indicator in Fig. 7.

It must be noted that this comparison of separate versus combined optimization is inherently unfair. The combined optimization contains the separate optimization space within itself, and so when taken to the limit must perform better. However, the separate approach converges faster so in cases where coupling is weak and the decomposition approach leads to a close-to-optimal solution, it can lead to gains in efficiency. Moreover, the decomposition approach is reflective of the treatment of this design problem in practice, where instruments and constellations are often designed independently of each other.

C. Science Value Optimization (Case 4)

The results of the science value optimization case are shown in Fig. 10. Figure 10 reveals that high science value (as measured by the remaining soil moisture retrieval error) was reached by relatively
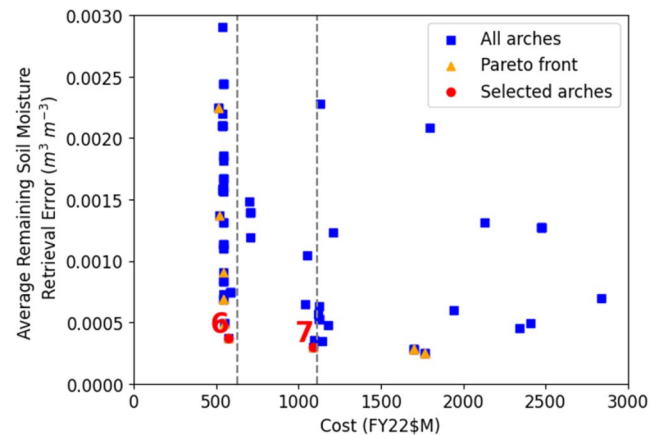

Fig. 10 Designs for the science value case.

Table 17   Selected architectures from the science value optimization, with vertical lines showing SMOS and SMAP cost caps

Architecture no.	n_s	n_p	h, km	i, deg	d_{az}, m	d_{el}, m	B_T, MHz	Δt_p, μs	Cost, FY22$M	Average soil moisture retrieval error, m^3 m^{-3}
6	1	1	998	87.2	10.9	13.0	22.3	44.7	577.8	3.71×10^{-4}
7	1	1	964	70.0	14.5	12.9	36.2	58.3	1089.9	2.96×10^{-4}

Table 18   Example architecture from the science value optimization

Architecture no.	n_s	n_p	h, km	i, deg	d_{az}, m	d_{el}, m	B_T, MHz	Δt_p, μs	Cost, FY22$M	Average soil moisture retrieval error, m^3 m^{-3}
8	1	1	941	70.1	6.68	9.97	1.4	16.1	515.1	0.0022

cheap architectures, and the returns provided by more capable and expensive satellites diminished quickly. Selected architectures showing these traits are provided in Table 17.

It appears that while architectures with small antennas at high altitudes might achieve the constraint of 100% coverage, the value of their measurements is much lower than those with larger antennas. Architecture 8 in Table 18 shows an example of this design. This manifests as the steep improvement in performance within architectures around $500M. Marginal improvement is provided by architectures with lower orbits and very large antennas, but this comes at much greater cost.

Naturally, not all of the points will be observed by the satellite, because the observations here are based on the FOR and not the FOV. Intelligent schedulers are expected to task the optimal pointing of the FOV within the FOR. Other work [19] explores more carefully how realistic satellite operations can reduce soil moisture error. However, such time-intensive planning decisions are difficult to reconcile with a large design space as this paper focuses on, and so we have presented the results of this limited evaluation.

Only a marginal improvement in soil moisture retrieval error is observed at the higher cost cap. The better radar performance does not significantly reduce the error, at least according to the soil moisture measurement model currently in use. This science-value based approach suggests that the lower cost cap can produce nearly as useful of a mission as the higher cost cap for the chosen measurement, and the saved cost could be used to improve revisit and thus improve the capture of spatio-temporal variations in soil moisture. It should be noted that this science value model does not consider the impact of revisit on improving soil moisture retrieval error globally, and future work should consider the evolution of soil moisture over time.

IV.   Conclusions

This work has shown multiple optimization cases for the design of a soil moisture mission. The results of the optimization revealed that when considering coverage and instrument design metrics, satisfactory performance is possible at a lower cost cap of 629.3FY22$M, but a great improvement in both maximum revisit time and NESZ is available at a higher cost cap of 1.116FY22$B. When a science-value metric is used instead, the improvement offered by more expensive architectures is seen to be negligible. This finding supports the idea that science value must be carefully considered when designing satellite missions, and simply optimizing for instrument performance or revisit time may lead to over-designed satellite constellations.

Also of note is the advantage of including instrument design variables and constellation design variables in the same optimization. Because variables like orbit altitude can greatly affect both instrument and constellation performance, optimizing all at once is shown here to outperform separate optimizations. This reinforces common systems engineering knowledge that emphasizes communicating across design subsystems.

While this work has provided insights into the tradespace for this and similar problems, it is limited in scope. Firstly, the radar design and satellite designs are of low to medium fidelity, and some details are ignored, as it is typically the case in tradespace exploration, which emphasizes breadth of alternatives to modeling fidelity. Secondly, time and computational limitations meant that the coverage computations were restricted to a relatively coarse grid with a short simulation duration. We do not expect the main conclusions to change significantly with higher-fidelity simulations, we only note that the optimal designs may differ slightly. Thirdly, this work considered only the field of regard of the instrument, and not the true field of view. To consider the FOV, an intelligent planner should be added to the operational model of the spacecraft, which can be computationally expensive. Finally, the science value objective function used here (remaining soil moisture retrieval error) is only a proxy for a more complete understanding of the scientific utility of the measurements of the constellation, which would have to consider expected spatiotemporal fluctuations in soil moisture globally.

With these limitations in mind, future work should focus on more closely coupling the retrieved measurements to the science variable being studied. For example, a model of predicted soil moisture could be fed the radar retrievals based on a planning algorithm that maneuvers the satellites to ground points with the greatest uncertainty. This would allow for the optimization routine to more directly connect to the observable, as opposed to the proxies that we have used in this work.

Appendix: Supplementary Figures Supporting Optimization Settings
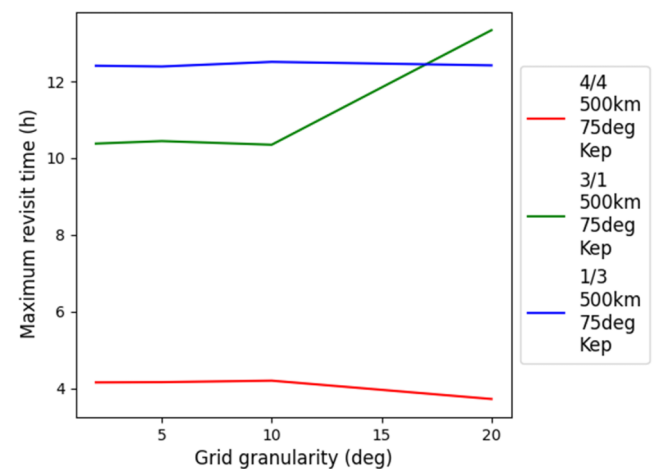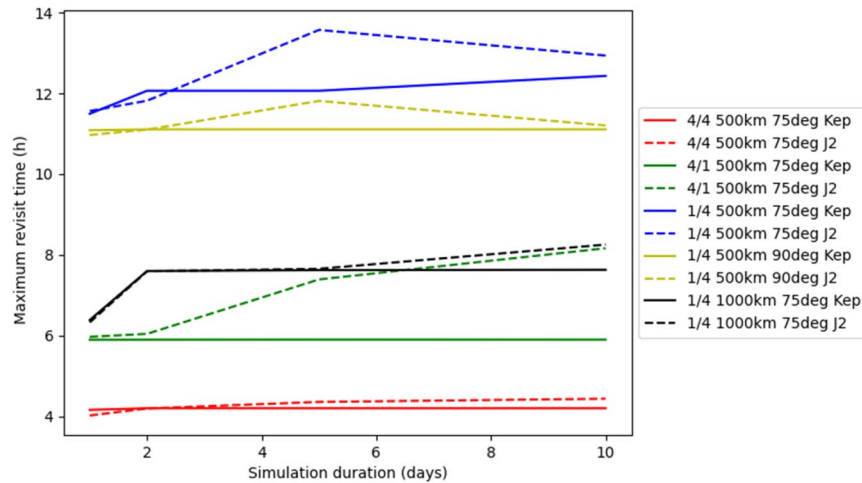

Fig. A1   Grid granularity study.

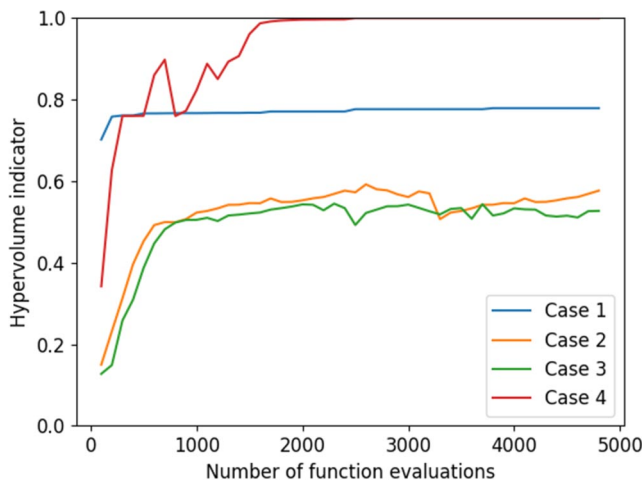**Fig. A2   Comparison of Keplerian and J2 propagators for various orbits.**

Fig. A3   Hypervolume indicators for various cases showing convergence around 2700 NFEs.

Acknowledgement

This work was supported by NASA (Grant No. 80NSSC20K1116).

References

[1] Kapurch, S. J., "NASA Program/Project Life Cycle," *NASA Systems Engineering Handbook*, Diane Publ., Pennsylvania, 2010.

[2] Ross, A. M., Hastings, D. E., Warmkessel, J. M., and Diller, N. P., "Multi-Attribute Tradespace Exploration as Front End for Effective Space System Design," *Journal of Spacecraft and Rockets*, Vol. 41, No. 1, 2004, pp. 20–28.
https://doi.org/10.2514/1.9204

[3] Ferringer, M. P., Clifton, R. S., and Thompson, T. G., "Efficient and Accurate Evolutionary Multi-Objective Optimization Paradigms for Satellite Constellation Design," *Journal of Spacecraft and Rockets*, Vol. 44, No. 3, 2007, pp. 682–691.
https://doi.org/10.2514/1.26747

[4] Hu, J., Huang, H., Yang, L., and Zhu, Y., "A Multi-Objective Optimization Framework of Constellation Design for Emergency Observation," *Advances in Space Research*, Vol. 67, No. 1, 2021, pp. 531–545.
https://doi.org/10.1016/j.asr.2020.09.031

[5] Xu, X., Ju, Z., and Luo, J., "Design of Constellations for GNSS Reflectometry Mission Using the Multiobjective Evolutionary Algorithms," *IEEE Transactions on Geoscience and Remote Sensing*, Vol. 60, June 2022, pp. 1–15.
https://doi.org/10.1109/TGRS.2022.3185776

[6] Dai, C., Zheng, G., and Chen, Q., "Satellite Constellation Design with Multi-Objective Genetic Algorithm for Regional Terrestrial Satellite Network," *China Communications*, Vol. 15, No. 8, 2018,

pp. 1–10.
https://doi.org/10.1109/CC.2018.8438269

[7] Budianto, I. A., and Olds, J. R., "Design and Deployment of a Satellite Constellation Using Collaborative Optimization," *Journal of Spacecraft and Rockets*, Vol. 41, No. 6, 2004, pp. 956–963.
https://doi.org/10.2514/1.14254

[8] Yan, D., You, P., Liu, C., Yong, S., and Guan, D., "Constellation Multi-Objective Optimization Design Based on QoS and Network Stability in LEO Satellite Broadband Networks," *KSII Transactions on Internet and Information Systems (TIIS)*, Vol. 13, No. 3, 2019, pp. 1260–1283.
https://doi.org/10.3837/tiis.2019.03.008

[9] Jilla, C. D., Miller, D. W., and Sedwick, R. J., "Application of Multidisciplinary Design Optimization Techniques to Distributed Satellite Systems," *Journal of Spacecraft and Rockets*, Vol. 37, No. 4, 2000, pp. 481–490.
https://doi.org/10.2514/2.3589

[10] Yi, H., Lei, W., Wenju, F., Haitao, Z., Tao, L., Beizhen, X., and Ruizhi, C., "LEO Navigation Augmentation Constellation Design with the Multi-Objective Optimization Approaches," *Chinese Journal of Aeronautics*, Vol. 34, No. 4, 2021, pp. 265–278.
https://doi.org/10.1016/j.cja.2020.09.005

[11] Golkar, A., Cataldo, G., and Osipova, K., "Small Satellite Synthetic Aperture Radar (SAR) Design: A Trade Space Exploration Model," *Acta Astronautica*, Vol. 187, 2021, pp. 458–474.
https://doi.org/10.1016/j.actaastro.2021.07.009

[12] Song, Z., Chen, X., Luo, X., Wang, M., and Dai, G., "Multi-Objective Optimization of Agile Satellite Orbit Design," *Advances in Space Research*, Vol. 62, No. 11, 2018, pp. 3053–3064.
https://doi.org/10.1016/j.asr.2018.08.037

[13] Saboori, B., Bidgoli, A. M., and Saboori, B., "Multiobjective Optimization in Repeating Sun-Synchronous Orbits Design for Remote-Sensing Satellites," *Journal of Aerospace Engineering*, Vol. 27, No. 5, 2014, Paper 04014027.
https://doi.org/10.1061/(ASCE)AS.1943-5525.0000340

[14] Pu, M., Wang, J., Zhang, D., Jia, Q., and Shao, X., "Optimal Small Satellite Orbit Design Based on Robust Multi-Objective Optimization Method," *Aerospace Science and Technology*, Vol. 70, Nov. 2017, pp. 339–350.
https://doi.org/10.1016/j.ast.2017.08.016

[15] Selva, D., Cameron, B. G., and Crawley, E. F., "Rule-Based System Architecting of Earth Observing Systems: Earth Science Decadal Survey," *Journal of Spacecraft and Rockets*, Vol. 51, No. 5, 2014, pp. 1505–1521.
https://doi.org/10.2514/1.A32656

[16] Siddiqi, A., Magliarditi, E., and de Week, O., "Valuing New Earth Observation Missions for System Architecture Trade-studies," *IGARSS 2019—2019 IEEE International Geoscience and Remote Sensing Symposium*, Inst. of Electrical and Electronics Engineers, New York, 2019, pp. 5297–5300.
https://doi.org/10.1109/IGARSS.2019.8899126

[17] Nag, S., Moghaddam, M., Selva, D., Frank, J., Ravindra, V., Levinson, R., Azemati, A., Aguilar, A., Li, A., and Akbar, R., "D-Shield: Distributed Spacecraft with Heuristic Intelligence to Enable Logistical Decisions," *IGARSS 2020—2020 IEEE International Geoscience and Remote Sensing Symposium*, Inst. of Electrical and Electronics

Engineers, New York, 2020, pp. 3841–3844.
https://doi.org/10.1109/IGARSS39084.2020.9323248

[18] Melebari, A., Nag, S., Ravindra, V., and Moghaddam, M., "Soil Moisture Retrieval from Multi-Instrument and Multi-Frequency Simulated Measurements in Support of Future Earth Observing Systems," *IEEE International Geoscience and Remote Sensing Symposium*, Inst. of Electrical and Electronics Engineers, New York, 2022.

[19] Levinson, R., Niemoeller, S., Nag, S., and Ravindra, V., "Planning Satellite Swarm Measurements for Earth Science Models: Comparing Constraint Processing and MILP Methods," *Proceedings of the International Conference on Automated Planning and Scheduling*, Vol. 32, AAAI Press, California, 2022, pp. 471–479.

[20] Sadeghi, M., Tabatabaeenejad, A., Tuller, M., Moghaddam, M., and Jones, S. B., "Advancing NASA's AirMOSS P-Band Radar Root Zone Soil Moisture Retrieval Algorithm via Incorporation of Richards' Equation," *Remote Sensing*, Vol. 9, No. 1, 2016, p. 17.
https://doi.org/10.3390/rs9010017

[21] Moghaddam, M., Rahmat-Samii, Y., Rodriguez, E., Entekhabi, D., Hoffman, J., Moller, D., Pierce, L. E., Saatchi, S., and Thomson, M., "Microwave Observatory of Subcanopy and Subsurface (MOSS): A Mission Concept for Global Deep Soil Moisture Observations," *IEEE Transactions on Geoscience and Remote Sensing*, Vol. 45, No. 8, 2007, pp. 2630–2643.
https://doi.org/10.1109/TGRS.2007.898236

[22] Ravindra, V., and Nag, S., "Instrument Data Metrics Evaluator for Tradespace Analysis of Earth Observing Constellations," *2020 IEEE Aerospace Conference*, Inst. of Electrical and Electronics Engineers, New York, 2020, pp. 1–20.
https://doi.org/10.1109/AERO47225.2020.9172705

[23] Maisonobe, L., Pommier, V., and Parraud, P., "Orekit: An Open Source Library for Operational Flight Dynamics Applications," *4th International Conference on Astrodynamics Tools and Techniques*, European Space Agency, Paris, 2010, pp. 3–6.

[24] Walker, J. G., "Satellite Constellations," *Journal of the British Interplanetary Society*, Vol. 37, Dec. 1984, p. 559.

[25] Selva, D., and Crawley, E. F., "VASSAR: Value Assessment of System Architectures Using Rules," *2013 IEEE Aerospace Conference*, Inst. of Electrical and Electronics Engineers, New York, 2013, pp. 1–21.
https://doi.org/10.1109/AERO.2013.6496936

[26] Wertz, J. R., Larson, W. J., Kirkpatrick, D., and Klungle, D., "Cost Modeling," *Space Mission Analysis and Design*, Vol. 8, Springer, New York, 1999.
https://doi.org/10.1007/978-94-011-3794-2

[27] Partridge, P., Moghaddam, M., Rahmat-Samii, Y., Haynes, M., van Nieuwstadt, L., Vitaz, J., Huang, J., and Cable, V., "A Dual Polarized UHF/VHF Honeycomb Stacked-Patch Array Antenna: Overview of an Enabling Technology for the MOSS Mission," *2008 IEEE Antennas and Propagation Society International Symposium*, Inst. of Electrical and Electronics Engineers, New York, 2008, pp. 1–4.
https://doi.org/10.1109/APS.2008.4619069.

[28] Habib-Agahi, H., Mrozinski, J., and Fox, G., "NASA Instrument Cost/Schedule Model," *2011 Aerospace Conference*, Inst. of Electrical and Electronics Engineers, New York, 2011, pp. 1–19.

[29] Deb, K., Pratap, A., Agarwal, S., and Meyarivan, T., "A Fast and Elitist Multiobjective Genetic Algorithm: NSGA-II," *IEEE Transactions on Evolutionary Computation*, Vol. 6, No. 2, 2002, pp. 182–197.
https://doi.org/10.1109/4235.996017

[30] Agte, J., De Weck, O., Sobieszczanski-Sobieski, J., Arendsen, P., Morris, A., and Spieck, M., "MDO: Assessment and Direction for Advancement—An Opinion of One International Group," *Structural and Multidisciplinary Optimization*, Vol. 40, No. 1, 2010, pp. 17–33.
https://doi.org/10.1007/s00158-009-0381-5

[31] Pereira, F., Reed, P. M., and Selva, D., "Multi-Objective Design of a Lunar GNSS," *NAVIGATION: Journal of the Institute of Navigation*, Vol. 69, No. 1, 2022.
https://doi.org/10.33012/navi.504

[32] Agrawal, R., and Srikant, R., "Fast Algorithms for Mining Association Rules," *Proceedings of 20th International Conference on Very Large Data Bases, VLDB*, Vol. 1215, Morgan Kaufmann, California, 1994, pp. 487–499.

[33] Zitzler, E., Brockhoff, D., and Thiele, L., "The Hypervolume Indicator Revisited: On the Design of Pareto-Compliant Indicators via Weighted Integration," *International Conference on Evolutionary Multi-Criterion Optimization*, Springer, New York, 2007, pp. 862–876.
https://doi.org/10.1007/978-3-540-70928-2_64

C. N. McGrath
Associate Editor